Transport and analysis of electron beams from a laser wakefield accelerator in the 100 MeV energy range with a dedicated magnetic line.

A. Maitrallain[a,*], T.L. Audet[b], S. Dobosz Dufrénoy[a,*], A. Chancé[c], G. Maynard[b], P. Lee[b], A. Mosnier[c], J. Schwindling[c], O. Delferrière[c], N. Delerue[d], A. Specka[e], P. Monot[a], B. Cros[b]

[a] *LIDYL, CEA-Saclay, CNRS, Université Paris-Saclay, 91191 Gif-sur-Yvette Cedex, France*
[b] *LPGP, CNRS, Univ Paris-Sud,Université Paris-Saclay, Orsay, France*
[c] *IRFU, CEA-Saclay, Université Paris-Saclay, 91191 Gif-sur-Yvette Cedex, France*
[d] *LAL, CNRS, Univ Pari-Sud, Université Paris-Saclay, Orsay, France*
[e] *LLR, CNRS, Ecole Polytechnique, Palaiseau, France*

Abstract

Electron bunches generated by laser driven wakefield acceleration are transported and analyzed using a magnetic line composed of a triplet of quadrupoles and a dipole. Short pulse bunches with a total charge of $\approx$ 130 pC, and broad band energy spectra in the range 45 to 150 MeV are generated by ionization assisted injection in a gas cell. The electron source is imaged about one meter away from the exit of the gas cell by the magnetic line, delivering electron bunches at a stable position in the image plane where a charge density of $\approx$ 2.9 pC/mm^2 at an energy of 69.4$\pm$0.6 MeV is achieved. This magnetic line improves dramatically the accuracy of energy determination of this electron source, leading to an energy error as low as 8.6 ‰ in the 70 MeV range for 5 mrad divergence electron bunch and considering the resolution of the entire detection system. The transport of bunches with improved stability and energy selection paves the way to various applications including multi-stage laser plasma acceleration.

Keywords: Laser wakefield acceleration, Transport line, Spectrometer

*Corresponding authors
Email addresses: antoine.maitrallain@strath.ac.uk (A. Maitrallain), sandrine.dobosz@cea.fr

1. Introduction

Since the first experimental demonstration of peaked electron spectra in 2004 [1, 2, 3] the field of laser driven wakefield accelerator (LWFA)[4] has achieved tremendous progress in the understanding of physical mechanisms and improvement of electron beam quality.

Electron sources generated in LWFA rely on the non linear interaction of the laser pulse with plasma electrons. Several processes were envisaged to improve the beam quality and stability, such as ionization injection [5, 6, 7], the use of colliding pulses [8], shock-induced density transition [9, 10] and density down-ramps injection [11] for example. Although promising results [12, 13, 14] have already been achieved towards selecting the beam energy and reducing the energy spread, divergence or conserving the emittance [15, 16], additional beam manipulations are required for most of the future applications of these compact sources.

Controlling and optimizing the electron beam properties is of primary importance for several applications such as the generation of high energy photons [17, 18] and very high energy electrons (VHEE) for medical treatment [19, 20, 21]. The multi-stage laser plasma accelerator scheme [22, 23, 24, 25] is also a promising option towards ultra-high energy compact accelerators. In the double stage version of this scheme, short electron bunches are injected into an accelerating plasma structure, providing multi-GeV energy gain to electrons in phase with the plasma accelerating field. Electron injection in this type of structure is one of the current challenges as it requires micron scale and femtosecond scale stabilization of electron bunches.

It is thus crucial to test ways to improve the quality and stability of electron beams generated by LWFA. The capability to transport and refocus electron beams from LWFA, counterbalancing their divergence, is as essential as being able to control their reproducibility. The pointing instability which could be observed experimentally comes from a combination of several contributions like the fluctuations of the laser position but also the temporal

(S. Dobosz Dufrénoy)

contrast of the laser pulse [26], the type of target used to generate the electron beam (gas jet, gas cell, capillary...) [27] for instance or the conditions of injection of the electrons in the accelerating cavity and its evolution [28, 29]. As soon as the electron beam exits the plasma, its size increases drastically and it needs to be controlled by appropriate transport components. Beam manipulation has already been tested using plasma lenses [30, 25, 31] as well as magnetic devices such as permanent magnet quadrupole (PMQ) to refocus the bunch [17, 32, 33, 34, 35, 36, 37, 38]. Several multi-petawatt laser facilities should be available soon so there is a need to test ways to transport the electron bunches between stages in the double stage acceleration scheme. This paper focuses on the analysis of the transport of an electron beam with broad energy distribution and divergence as easily achieved by LWFA.

In addition, the transport of the electron beam provides a way to separate electrons from radiation exiting the plasma. In a laser plasma injector, the laser beam and electron bunch copropagate on the same axis. For applications, it is desirable to use the electron bunch in the absence of laser or betatron radiation which can modify the sample. For example in the context of sample irradiation for biological studies or dynamical structural material property studies [39], an electron beam size of typically 1 mm full width at half maximum (FWHM) is required. Placing the sample close to the plasma exit where this beam size is achieved would expose it to laser radiation typically with an intensity of the order of 10^{13} W/cm^2, strong enough to induce damages in most materials. Transporting and imaging the electron beam away from the plasma exit, and separating it from radiation is thus essential for applications.

A magnetic line was specifically built to stabilize and analyze a LWFA electron beam [40, 41, 42] available on a 100 TW class laser facility. It was designed taking into account realistic parameters and experimental constraints of the facility (room size, chamber size, other implemented diagnostics), to transport the largest amount of charge at an energy around 70 MeV and obtain in the image plane a beam size of the order of the source size, with two objectives. The first is to perform preliminary studies of beam transport in view

of future two-stage acceleration experiments in preparation at the Apollon laser facility [43]. The second is to manipulate and deliver the bunch for applications [19, 20, 21] : it implies to transport the electron beam from the laser focal plane, stabilize and focus it, maintaining a maximum charge density for sample irradiation.

In this paper, we demonstrate the feasibility of using this magnetic line for LWFA electrons with broad energy spread and of delivering a large charge density over mm^2 areas for applications. Bunches are generated by ionization assisted injection in a short length plasma, with a relatively large charge and divergence, of the order of 10 mrad. The magnetic line is used to characterize the electron beam properties and achieve a stable electron beam with a high charge density in a narrow energy range (≈ 2.9 pC/mm^2 at 69.4 MeV $\pm$0.6 MeV).

The charge transmission was measured and the electron beam spectrum was analyzed with and without the magnetic transport line. The effects of the magnetic line on the beam size, charge, shot-to-shot stability and on the measured energy spectrum are discussed.

The remainder of the paper is organized as follows. In section 2 the characteristics and performances of the transport line are described; simulations using a uniform electron distribution at the entrance of the line allow us to determine the electron distribution at the output; the method used to reconstruct the input electron spectrum from the measurements is described. Section 3 describes the experimental set-up and results, either using a single dipole, or the whole transport line to diagnose the electron beam.

2. Transport line characteristics

A magnetic line was designed to image and characterize the electron beam properties such as energy distribution and angular divergence. In order to build a compact line, located close to the electron source inside the vacuum chamber, permanent magnets were preferred to electro-magnets. The sensitivity to electron beam pointing fluctuations were minimized. To do so the 6×6 transfer matrix R defining the relation between the initial and final

electron coordinates (characterized by its position and divergence in the x and y direction, its arrival time and relative energy difference denoted by (x, x', y, y', $dl = -cdt$, δ)) from the plasma exit to the observation point has the values $R_{12} = R_{34} = 0$ for the reference energy of 70 MeV. This corresponds to the astigmatism conditions and means that the final horizontal (vertical) position does not linearly depend on the initial horizontal (vertical) angle. The sensitivity to the electron beam pointing fluctuations is then reduced. Moreover, the implementation requires a minimum distance of 160 mm between the first magnet and the plasma exit. We have chosen to use a triplet instead of a doublet for the focusing to balance the betatron functions in the quadrupoles (and thus the chromatic effects) and to have similar values of R_{11} and R_{33} at the observation point. R_{11} and R_{33} are defined as the relation between the beam final horizontal (vertical) position with its initial horizontal (vertical) position. A dipole is then inserted downstream of the triplet to perform the spectral analysis.

The transport line is made of a quadrupole triplet located at 160 mm from the plasma cell exit and a 120 mm-long dipole. The outer quadrupoles of the triplet are 80 mm long and the inner quadrupole is 120 mm long with an inter-distance of 60 mm. Each element length is a multiple of 40 mm which enables using the same blocks. The focal plane, where the Lanex screen is inserted, for electrons reference energy (70 MeV) is about 1 m away from the source. For the line design, the quadrupole and dipole field maps were computed with the OPERA software [44]. After construction, the magnetic field was measured at discrete positions with a Hall probe. Finally, the field maps were calibrated with measured values and used for all simulations presented below.

2.1. Simulation of transport with electron distribution

TraceWin [45] simulations show that 1 m away from the source the magnification factor is 1.1 in the horizontal plane, and 2 in the vertical one for the reference energy. When the dipole is used after the triplet, focusing forces in the vertical plane (due to the triplet) and

dispersive ones in the horizontal one (due to the dipole), result in a distribution of electrons in the focal plane asymmetrically diverging on each side of the pinch position which is located at 70 MeV, the reference energy of the line.

In experimental conditions allowing us to generate a high charge around 70 MeV as described in section 3.1, the large angular distribution induces uncertainty on the energy determination. To reduce the error in the energy measurement, the divergence was limited to $\pm$ 5 mrad at the entrance of the transport line using a circular tungsten collimator. The choice of this value was guided by the fact that it transmits a sufficient amount of charge of the order of a few % and allows to limit geometrical and chromatic aberrations induced by electrons impinging at large angles ($>$ 10 mrad). One can note that the use of the collimator does not affect the pointing fluctuations of the source (see part. 3.3.1). Indeed, experiments were conducted with one showing a larger radius ($\pm$10 mrad acceptance) and even without collimator (electrons go through the 40 mm aperture or 250 mrad of the first quadrupole) and gave similar results in terms of position stability in the detection plane.

To reproduce our experimental electron source, we assume a source size (radius $1/e^2$) of 1.5 µm and consider electrons in the range between 45 and 150 MeV and a (RMS) divergence of 20 $\times$ 10 mrad (horizontal axis $\times$ vertical axis). The transport of such a distribution was simulated, with a divergence of $\pm$ 5 mrad to account for the collimator. The resulting density of electrons is plotted in FIG. 1 as a function of the evaluated energy and vertical position in the focal plane of the transfer line. The evaluated energy corresponds to the energy measured with the spectrometer and not necessarily to the energy of the electrons at the entrance of the line.

This simulation takes into account the experimental resolution of the Lanex Regular screen [46] of the order of 100 µm. It shows that the electronic distribution obtained in the image plane exhibits an asymmetrical "butterfly" shape, with a pinch position at 70 MeV as expected and a pinch size of 200 µm FWHM.

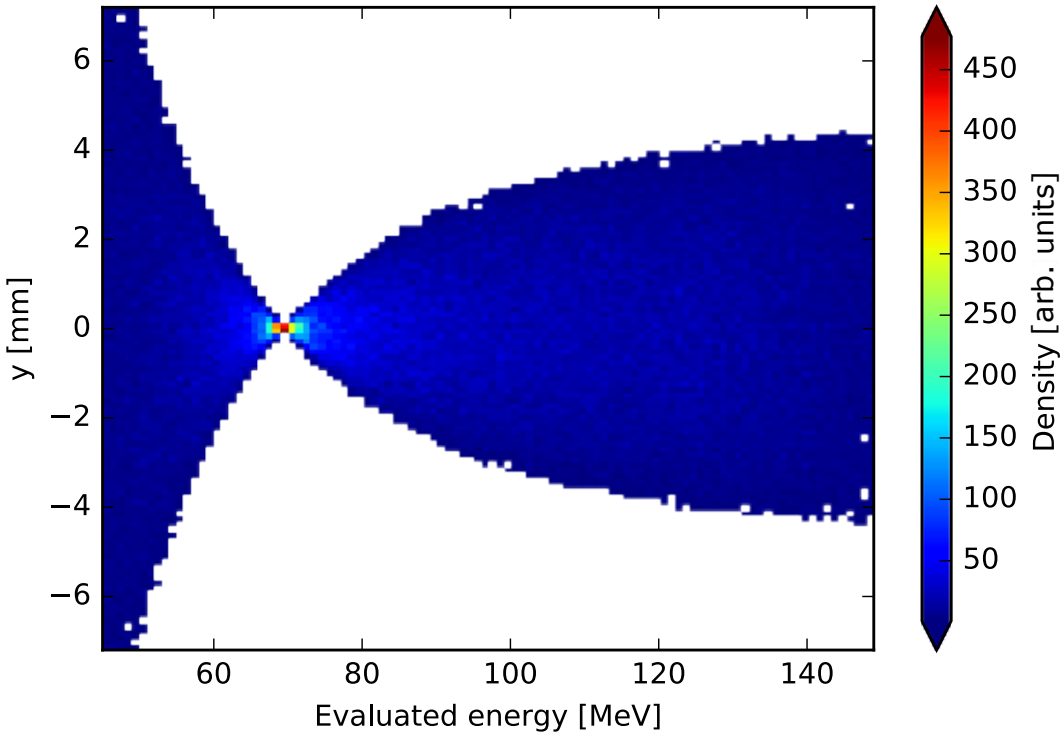

Figure 1: Electron distribution in the image plane of the magnetic transport line including dipole for an energy distribution uniform between 45 and 150 MeV.

The simulation of the quadrupole triplet response was performed with TraceWin for a realistic energy range (from 45 MeV to 150 MeV by 0.1 MeV steps) and various angles (over a disk of radius 5 mrad by 1 mrad steps) at the entrance of the line. This was used to evaluate the size and divergence of the electron distribution at the Lanex screen located in the focal plane of the magnetic line. After their travel through the triplet only, the electron vertical position and angle on the Lanex screen in the focal plane of the transport line are plotted as functions of their energy in FIG. 2a) and b) for different values of the initial divergence, considering the horizontal and vertical one are the same.

It shows that electrons with a zero divergence at the source (black lines in FIG. 2) are not deviated in the vertical plane for energies in the range 45 MeV to 150 MeV. All the curves in FIG. 2a) cross the axis for 70 MeV whereas they cross it at 79 MeV in 2b). Assuming there

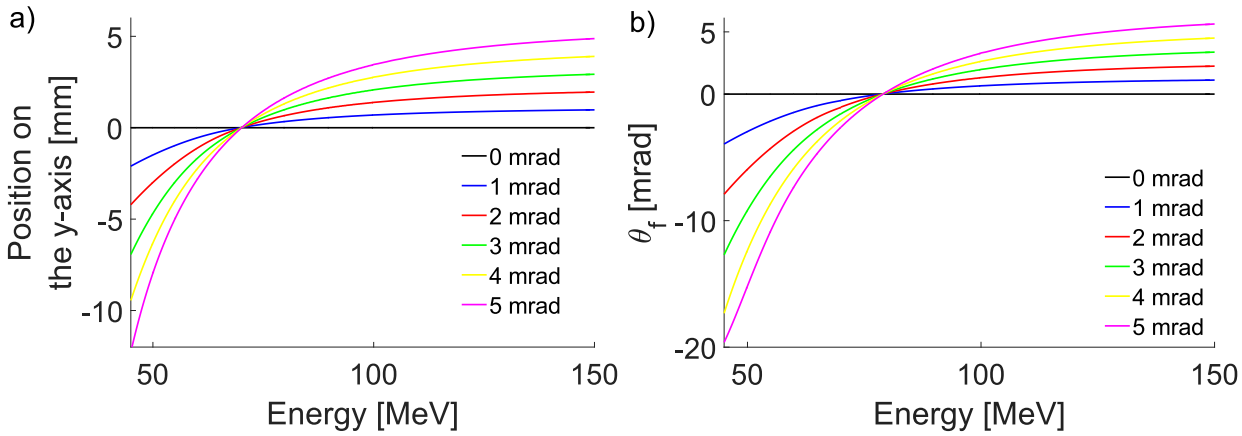

Figure 2: Final vertical position a) and angle b) of the electrons as a function of energy in the range 45 MeV to 150 MeV, for a set of initial divergence values indicated in the legend, on the Lanex screen in the focal plane of the transport line.

is no correlation between the angle and the position, it means that for energies between 70 MeV and 79 MeV the electron trajectories are converging (the vertical angle and position have opposite signs) whereas outside this energy range the beam is divergent in the vertical direction. These results show that electrons with energy lower than 70 MeV have a larger divergence and deviation than electrons with higher energies, which are less deviated by the transport line. This behavior is all the more pronounced for larger values of the initial divergence. This explains the asymmetry of the distribution observed in FIG. 1.

2.2. Energy determination with the triplet and dipole system

In this section we show how the accuracy of the transport line and the energy distribution of electrons at the entrance are determined.

The energy error as a function of the nominal energy for a given divergence can be calculated using Tracewin simulations of any known electron population transported through the triplet and the dipole. Simulations of transport through the triplet and the dipole were performed for the same parameters as the one used for FIG. 2. The dispersion function of the transfer line is computed from the position in the focal plane of electrons incident on axis. Then considering diverging electrons at the entrance, the energy error was computed

as the position difference between the diverging and non diverging electrons at a given energy. The energy error ΔE/E, defined as the ratio of the error ΔE to the energy, E, of the characterization line only, is plotted in FIG. 3 as a function of the energy for different initial values of the electrons horizontal divergence.

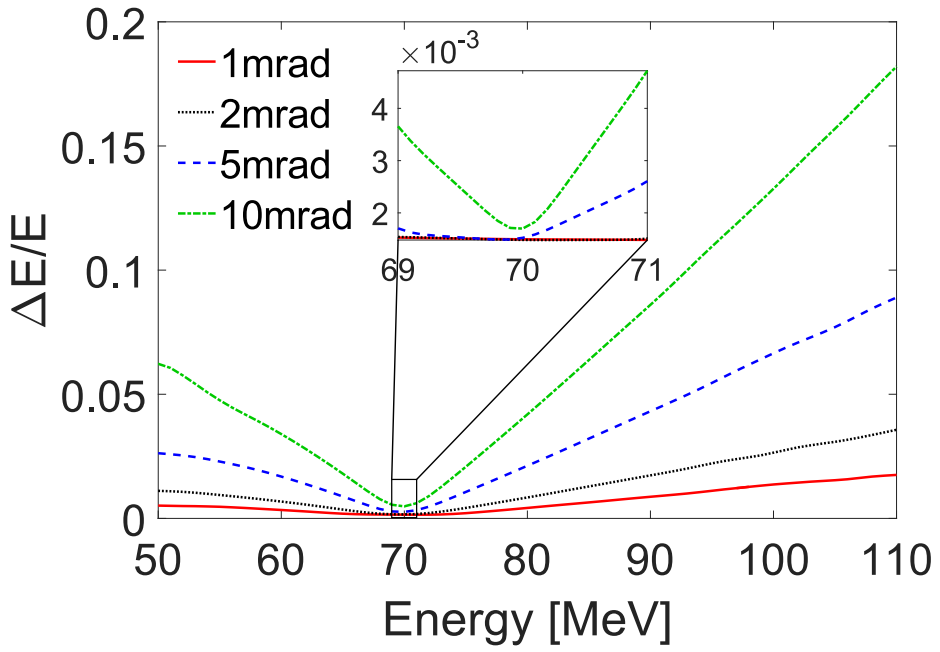

Figure 3: Energy error as a function of energy for different initial divergence of the electrons. The inset is a zoom between 69 MeV and 71 MeV.

As expected the smallest error is obtained at the reference energy (≈ 70 MeV) and is as low as 1.5 ‰ for a 1 mrad and 1.7 ‰ for 10 mrad divergence. Taking into account the imaging resolution, the energy error is increased to 8.6 ‰ in the reference energy range.

The charge density distribution by energy unit at the output of the transport line, $P_{out}(E)$, is calculated as the product of the distribution at the entrance, $P_{in}(E)$, and the transfer function of the transport line such as :

$$P_{out}(E) = \int P_{in}(u) F_R(E_{out}, E_{in}) dE_{in} \,, \tag{1}$$

with $\mathrm{F}_R(E_{out}, E_{in})$ that can be defined as the transfer function of the line normalized by :

$$\int_E F_R(E_{out}, E_{in})dE = 1$$

where E_{in} is the energy of the electron before the line and E_{out} the one evaluated at the output.

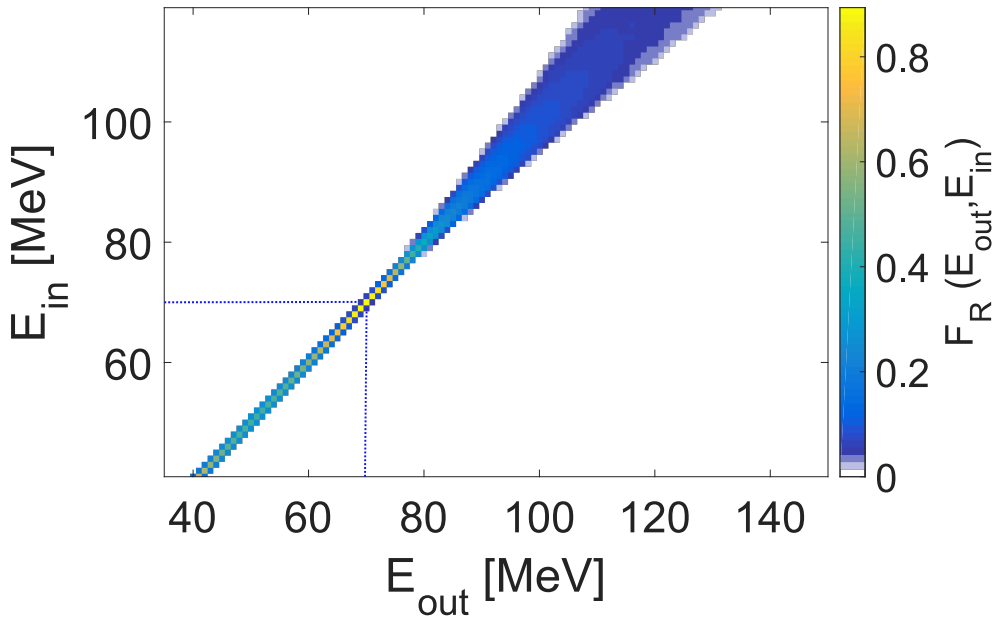

Figure 4: Transfer function of the transfer line in the input - evaluated output energy plane. The blue dotted vertical and horizontal line indicate the value 70 MeV, where the maximum of $F_R(E_{out}, E_{in})$ is located.

TraceWin simulations were performed to determine the electron charge density distribution by energy unit before and after the line. Then the transfer function was calculated using Monte Carlo simulations with a 1 MeV step grid, and assuming that the electron distribution is uniform over a disk of 5 mrad radius. This last assumption is valid because the typical RMS divergence (of the order of 10 mrad) of the beam is significantly larger than the limitation at ± 5 mrad due to the collimator. The calculated transfer function is plotted in FIG. 4 in the input and output energy space.

FIG. 4 shows that the transfer function provides a determination of the output energy with the smallest error at (70 MeV ±1 MeV) and error lower than 10 % in the range $40 - 80$ MeV; then the error on the energy grows for energies larger than 80 MeV.

The spectrum at the entrance of the transfer line can then be reconstructed, using the calculated transfer function, and for example, an analytic function fitting a typical measured spectrum after the transfer line. The output spectrum and reconstructed spectrum at the entrance are plotted in FIG. 5 where the two curves are very closely superposed. This reconstruction is thus very accurate, demonstrating that this transfer line is a precise diagnostics to characterize the electron spectrum in this energy range.

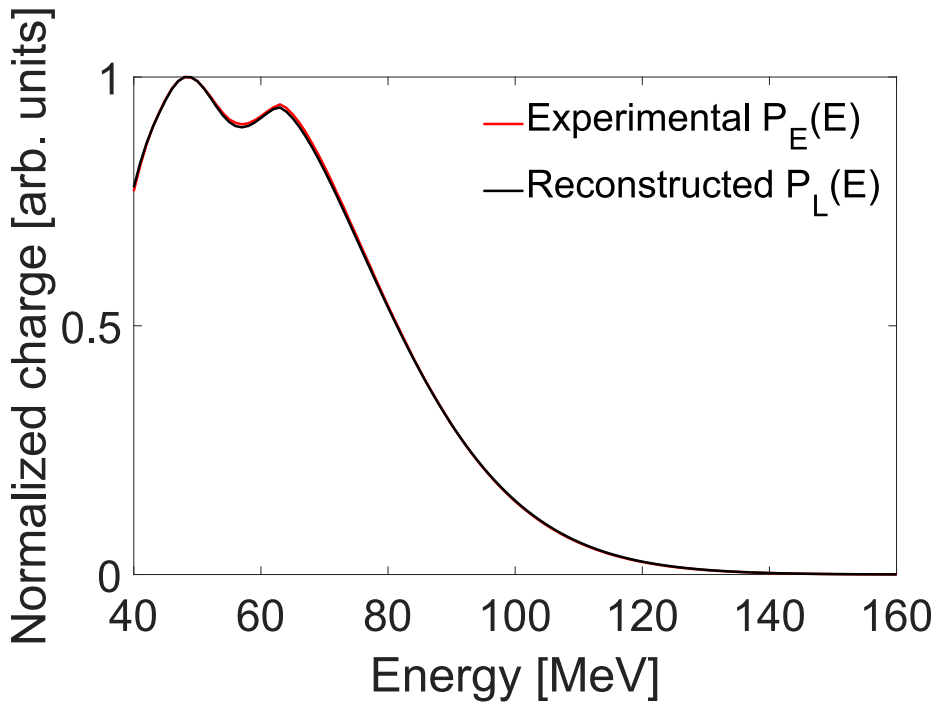

Figure 5: Measured spectrum (red line) after the magnetic line and reconstructed spectrum (black line) at the entrance as a function of electron energy.

3. Experimental results and discussion

3.1. Experimental set-up

Experiments were carried out using the UHI100 facility, a 100 TW class Ti:Sapphire laser system at CEA-Saclay. Linearly polarized laser pulses of (24 ± 1) fs duration (FWHM) are delivered at 800 nm center wavelength and 10 Hz repetition rate. A deformable mirror is used in order to correct the laser wavefront and obtain the most symmetrical distribution of the energy in the transverse focal plane under vacuum. The laser pulses were focused using a 1.1 m focal length off-axis parabola to a spot radius at $(1/e^2)$ of $(16\pm1\times15\pm2)$ μm^2 with 50% of energy within this surface. The total laser energy in the focal plane was on average $E_L = (0.95 \pm 0.13)$ J and the resulting estimated peak intensity was $I_L = (4.8 \pm 0.5) \times 10^{18}$ W/cm^2 which corresponds to a normalized laser amplitude of $a_0 = 1.5 \pm 0.1$.

Laser pulses were focused inside a variable length gas cell [41, 42] filled with a gas mixture composed of 99% H_2 and 1% N_2. Electron trapping is achieved by ionization assisted injection. The electronic density was tuned from 5.6×10^{18} e^-/cm^3 to 1.2×10^{19} e^-/cm^3 with a cell length of 500 μm $\pm$ 100 μm. A schematic view of the experimental set-up is presented in FIG. 6.

The relativistic electron bunches exiting the gas cell were characterized using two different configurations. As illustrated in FIG. 6a), in the first configuration, the transverse distribution of electrons was recorded directly after exiting the gas cell using a Lanex screen placed at 416 mm from the focal plane of the laser. The energy spectrum can be obtained by inserting in the path of the electron bunch a removable 55 mm-long magnetic dipole (configuration D) with a maximum field strength of 0.82 T. The exit face of the dipole is placed 120 mm before the Lanex screen (FIG. 6a)). In the second configuration, shown in FIG. 6b), a magnetic transport line, composed of a quadrupole triplet designed to focus 70 MeV electron beams, and a collimator to lower energy measurement error at 70 MeV is inserted in the beam path. The transverse distribution of the electron beam is determined

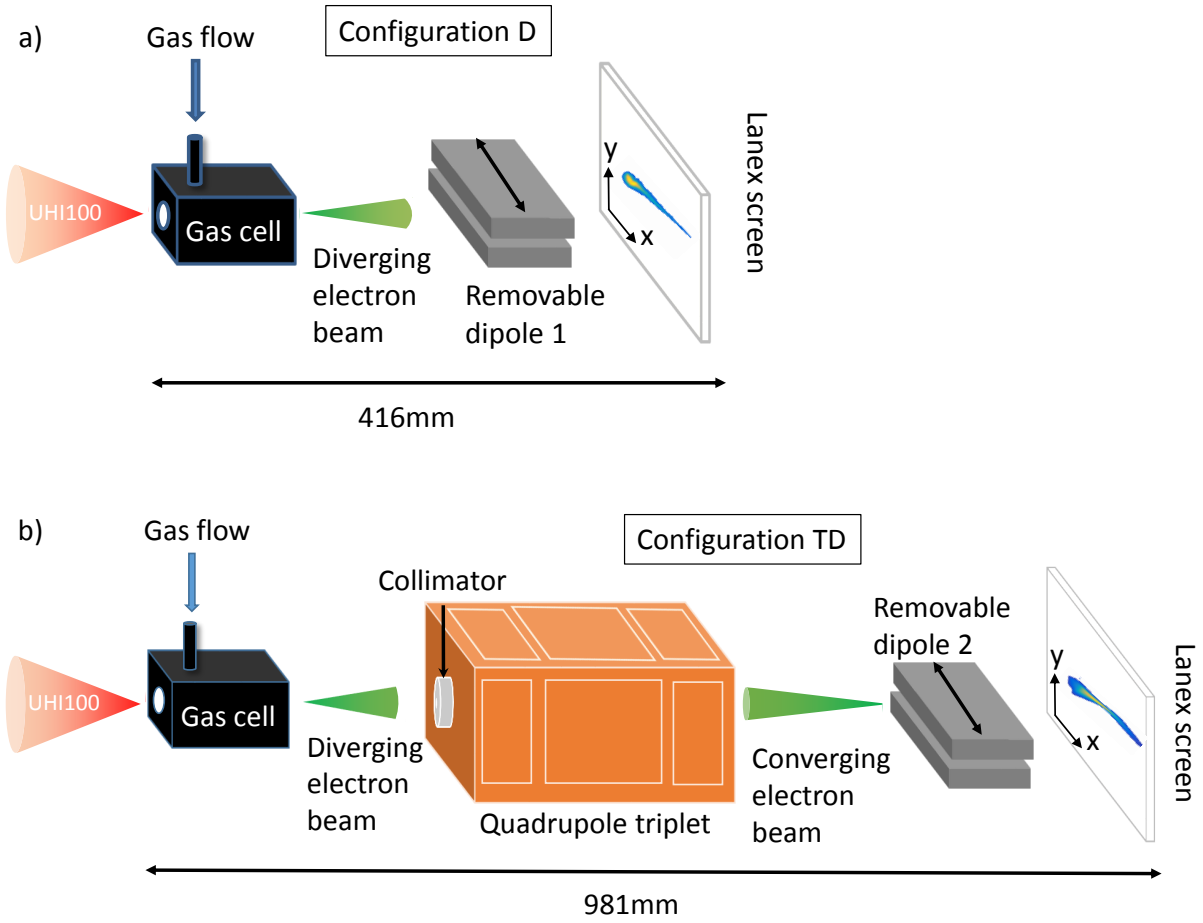

Figure 6: Schematic diagram of experimental set-up : a) the electron source can be diagnosed with a Lanex screen imaged onto a 16 bit CCD camera, and for the spectral part with a dipole inserted into the electron trajectory (configuration D) or b) the source can also be imaged using a magnetic line (a triplet of quadrupoles) and be diagnosed with a Lanex screen imaged onto the same 16 bit CCD camera and to obtain the spectral characteristics, a dipole could be inserted into the electron trajectory (configuration TD).

with a Lanex placed 981 mm after the focal laser plane corresponding to the focal plane of the triplet for 70 MeV electrons. The dispersion is achieved by a movable 120 mm-long dipole with a maximum field strength of 0.3 T, additionally inserted in front of this Lanex in configuration TD. Considering the effective position of each magnetic element relative to the exit of the gas cell, the reference energy defined by the experiment set-up is 69.4 MeV, close to the 70 MeV design value.

Both Lanex screens (Regular by EDM- Imaging) were imaged on a 16 bit Roper Scientific

CCD and the charge was calculated using a previous calibration obtained with a conventional electron source (ALIENOR CEA-Saclay [47]). The lowest energy that can be measured, due to the imaging cut off, is ≈ 20 MeV (in configuration D) or ≈ 38 MeV (in configuration TD). In order to avoid taking into account the signal near the cutoff of our experimental devices, only electrons above 45 MeV were considered for the following analysis.

3.2. Electron beam characterization

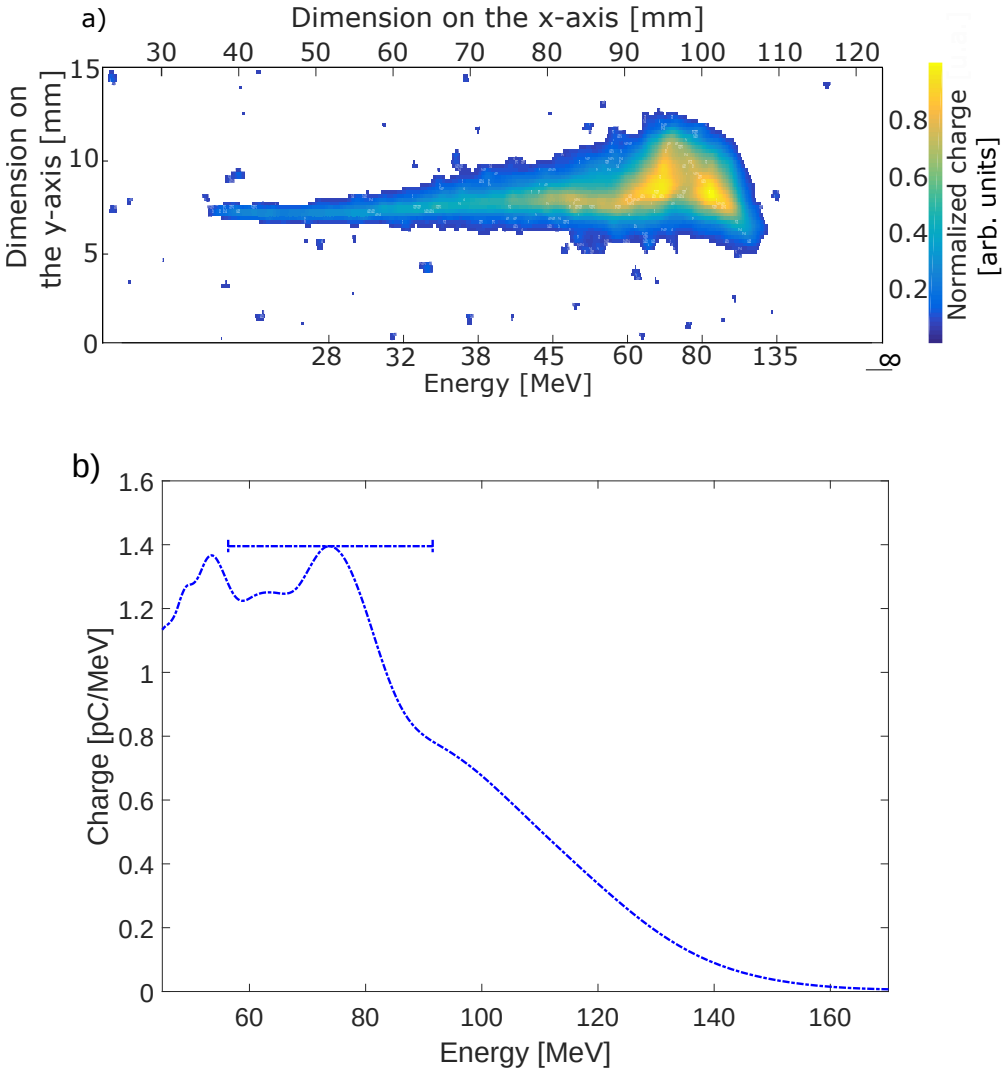

Figure 7: Typical electron distribution recorded on the Lanex screen at 416mm after the laser focal plane as a function of energy (configuration D) a) and associated spectrum b).

For an electronic density of $n_e = 7.5 \times 10^{18}$ e^-/cm^3, the laser focused at 0.6 mm before the entrance of the cell with the set-up described above in FIG. 6a), electron beams have, on average over 5 shots, a total charge of 132 pC, a mean size of $(x \times y) = (6.4 \times 3.0)$ mm^2 (FWHM) and a pointing fluctuation of (0.47×1.2) mm^2 (RMS). For these results and in the following of the paper, the x−axis (y−axis) denotes the horizontal (respectively vertical) axis. The divergence is larger on the x−axis because it is the laser polarization axis [48].

An example of electron distribution recorded on the Lanex screen in configuration D is shown in FIG. 7a) and the corresponding energy spectrum, summed in the vertical direction, in FIG. 7b). In these experimental conditions the spectrum, averaged over 3 shots, is peaked at 69 MeV ±17.6 MeV with a total charge of 50.6±8.6 pC in the energy range [45−150] MeV. In FIG. 7a) the apparent increase of the transverse size of the beam with the increase in energy up to 60 MeV, is only due to the increase of the Lanex signal with the number of electrons, which is increasing with energy up to 60 MeV. As expected from ionization induced injection mechanism, the spectrum is broad, with, in this experimental conditions, electrons up to a maximum energy of about 130 MeV. This energy is defined as the energy where the signal $I_{E_{max}}$ reaches 10% of the peak energy signal, $I_{E_{peak}}$, such as $I_{E_{max}} = I_{E_{peak}}/10$. The energy dependent uncertainty on the energy determination can be computed for known divergence and fluctuations. It is represented by the horizontal error bar at the maximum of the spectrum in FIG. 7b).

3.3. Electron beam diagnostic with the magnetic line

3.3.1. Distribution of electrons in the focal plane

Transverse electron distributions are plotted in FIG. 8, corresponding to an electron beam freely diverging after exiting the plasma, FIG. 8a), and focused by the triplet, FIG. 8b) for a series of shots with $n_e = 7.5 \times 10^{18}$ e^-/cm^3, and the laser pulse focused at 0.5 mm before the entrance of the cell. A single distribution is shown for each configuration and red crosses indicate the barycentres of 8 shots (FIG. 8a)) without and 9 shots (FIG. 8b))

with the transport line. Averaged values relative to these data are given in table 1. In this table, the size and shot-to-shot fluctuations in configuration TD, 981 mm after the source, are compared to the freely diverging beam, extrapolated from the measurements performed in configuration D, 416 mm after the source.

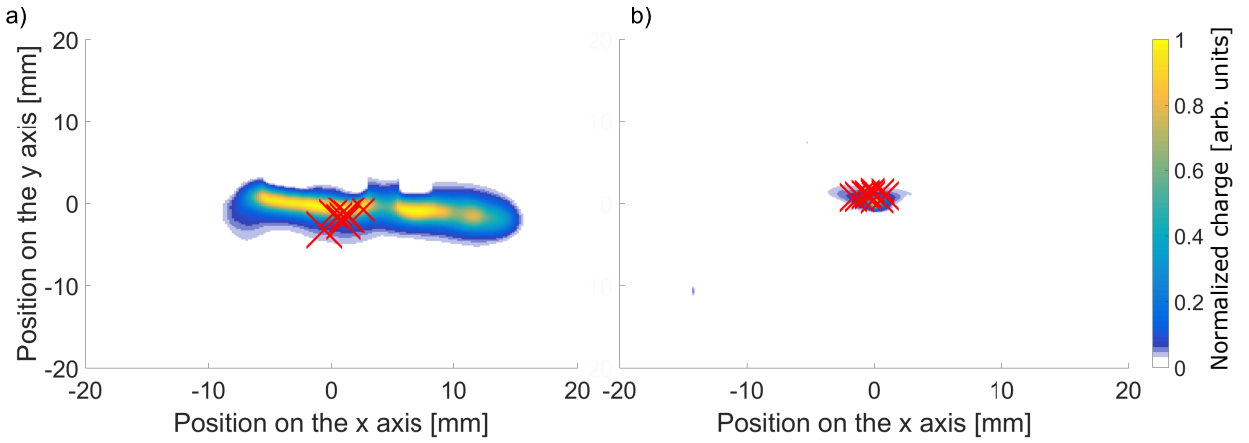

Figure 8: Electron beam transverse distribution on Lanex screens a) 416 mm after the laser focal plane without triplet b) on the focal plane of the transport line. One transverse distribution is shown and the red crosses correspond to the barycentres for a series of shots under the same conditions.

	RMS Pointing fluctuations [mm] $(x \times y)$	FWHM Size [mm] $(x \times y)$	Charge [pC]
Freely diverging (see FIG. 8a))	2.2×1.8	23×6.6	81.3 ± 11
Focused electrons (see FIG. 8b))	0.82×0.31	1.3×0.87	5.3 ± 2.2

Table 1: Electron transverse distribution properties of both the freely diverging and focused electron beam under the same experimental conditions, corresponding to the data of FIG 8.

These data show that imaging the electron beam improves its properties for applications in the focal plane of the triplet for the reference energy. For the freely diverging beam, we retreive the large x-y asymmetry with the size in the x direction being 3.5 larger than the y one. This value of ratio is in good agreement with the one found in numerical simulation for similar laser and target configuration [49]. Comparing the properties of the freely diverging electron bunches at 981 mm after the source, and those of the focused beams at the same

position, the shot-to-shot (RMS) fluctuations are reduced by a factor 2.7×5.7 and the size (FWHM) by a factor 18×7.6. The mean transported charge is 6.5% of the initial charge, reduced by the collimator, eliminating electrons outside the ± 5 mrad angle.

The size of the electron bunch measured in the focal plane is $((1.3 \pm 0.5) \times (0.87 \pm 0.2))$ mm^2 (FWHM). These values are in reasonable agreement with the ones expected from a broad distribution, as the focusing distance of the triplet is energy dependent and this results in an enlarged spot size. Considering the spectral (as given in Fig. 7b)) and spatial (cut to ± 5 mrad divergence from the source presented in the previous section) properties of the beam, the size in the focal plane is estimated to be (0.56×0.89) mm^2 spot (FWHM). The observed difference beetwen the measured and the estimated values of the beam size in the x direction can be attributed to the contribution of low energy electrons (< 45 MeV), not included in the estimated value and which divergence is more sensitive to the laser polarisation direction. This point will be investigated in more details in a forthcoming experiment.

3.3.2. Electron beam diagnostic with the triplet and dipole

The electron beam spectral distribution was measured after the transport line equipped with the dipole (configuration TD). A typical image and the corresponding spectrum are shown in FIG. 9. The electron distribution in the focal plane exhibits a pinched shape as expected in configuration TD and shown in FIG. 1 at exactly the theoretical energy given for the implemented set up (69.4 MeV). FIG. 9b) shows there is a good agreement between the peak energy measured before and after transport.

Characteristic parameters related to the electron spectra obtained in configurations D (blue curve in FIG. 9b)) and TD (red curve in FIG. 9b)) under the same experimental conditions ($n_e = 1.2 \times 10^{19}$ e$^-$/cm^3 and the laser is focused 0.8 mm before the entrance of the cell), are compared in table 2. The vertical size at a distance of 981 mm after the source for the freely diverging beam is extrapolated from the measurements performed in

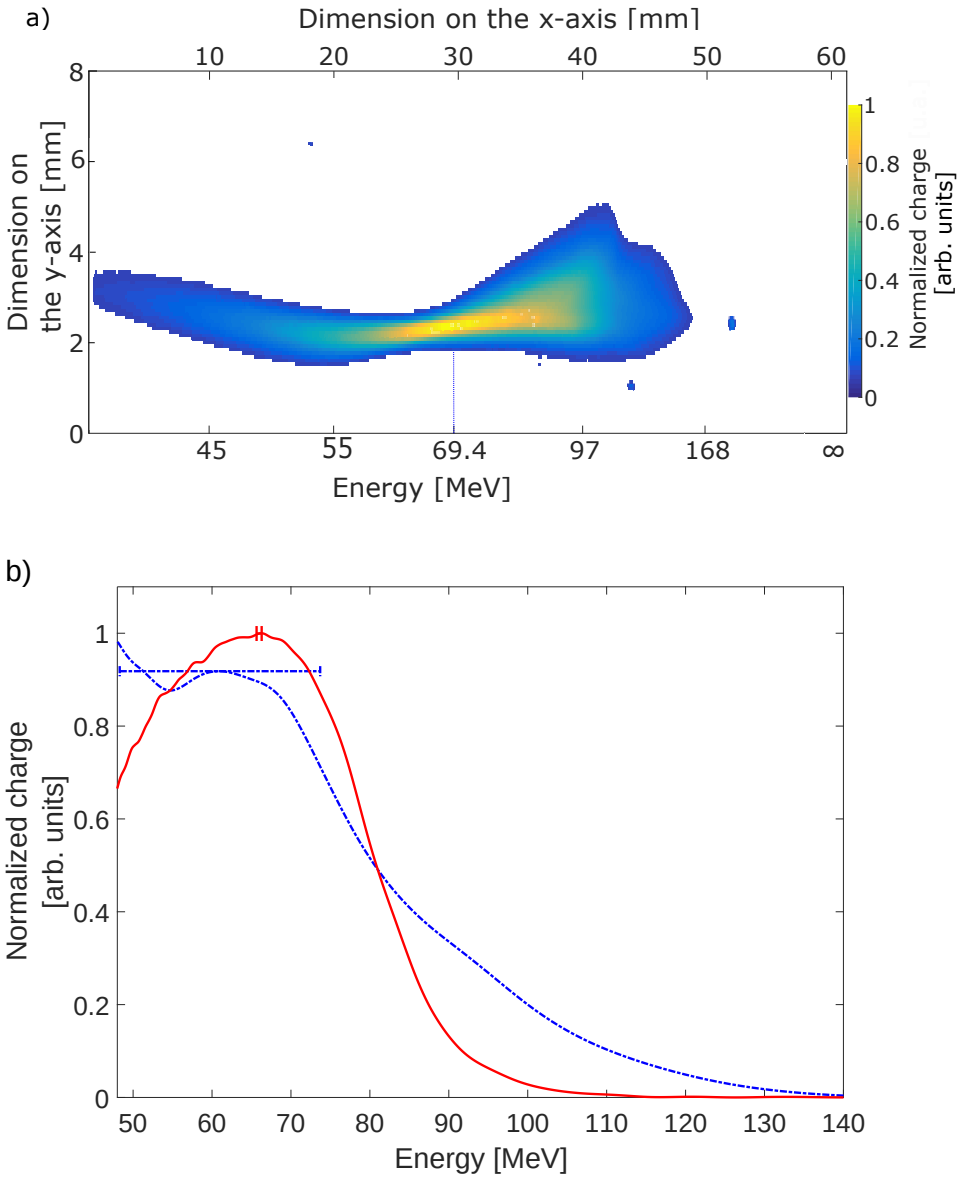

Figure 9: Electron spectrum a) on the Lanex on the focal plane of the transport line 981 mm after the laser focal plane (through TD) b) Averaged spectrum over a series of shots under the same conditions in dotted blue line : 416 mm after the source without transport (normalized to 2.02 pC/MeV), in solid red line : after transport by the magnetic line (normalized to 0.13 pC/MeV).

configuration D (at 416 mm), assuming linear evolution.

The average vertical size of the focused electron beam is reduced by a factor 8.5 and the transported charge is $(8.4 \pm 6.9)\%$ of the measured charge in the 45 MeV to 150 MeV energy range.

	Charge (between 45MeV and 150 MeV) [pC]	Vertical size 981 mm after the source [mm]	Vertical size 981 mm after the source in the 70 MeV range [mm]
Freely diverging (see FIG. 9b) blue)	56 ± 20	6.4	7.5
Focused electrons (see FIG. 9b) red)	4.7 ± 2.2	0.75	0.57

Table 2: Table showing the electron spectrum properties of both the freely diverging and focused electron beam under the same experimental conditions.

The ratio between the electron beam size at the entrance of the triplet and the collimator entrance surface is 15.5% which is in agreement with the (8.4 ± 6.9)% experimental value. This means that the transmitted charge is of the order of the fraction of the electron beam which goes through the collimator.

From the analysis of the spectra on the Lanex screen images, it is possible to determine the position fluctuation and size in a given energy range. The vertical shot-to-shot position fluctuations in the 70 MeV region (70 ± 2 MeV in configuration TD and 70 ± 20 MeV in configuration D) is determined for these two sets of shots, which spectrum is reported in FIG. 9b). The wider energy range in configuration D is due to a larger energy error compared to configuration TD. The position fluctuation in this restricted energy range is 500 µm in configuration D and a value below the experimental resolution (≈ 125 µm in this configuration) for the TD one. The magnetic line reduces the vertical position fluctuations by at least a factor 4 around 70 MeV and the size by a factor ≈ 13 (see table 2).

FIG. 10 shows the variation of the vertical size of an electron beam passing through the magnetic transport line associated to the dipole as a function of its energy.

These data correspond to the smallest measured pinch size of $\approx 191 \pm 50$ µm (FWHM) at 69.4 MeV ± 0.6 MeV for $n_e = 8.9 \times 10^{18}$ e^-/cm^3 and a laser pulse focused 0.6 mm before the entrance of the cell. This result is in good agreement with the simulation results reported in Fig. 1 which predict 200 µm pinch size. The spatial resolution could be improved by the use of other scintillators such as a YAG crystal [50].

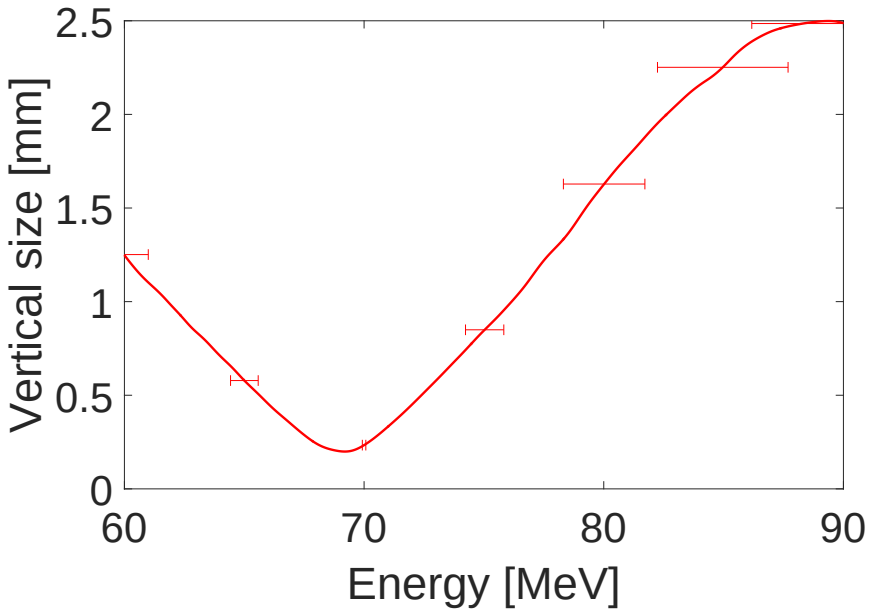

Figure 10: Variation of the vertical size (FWHM) of the electron beam as a function of its energy, in the focal plane of the triplet of quadrupoles, associated to the dipole for spectrum characterization.

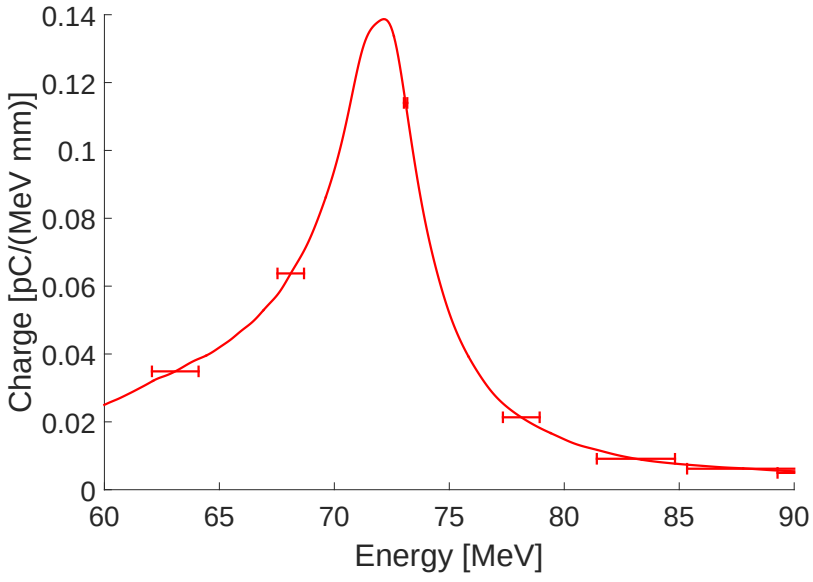

Figure 11: Electronic charge density calculated from the Lanex screen measurement, in the focal plane of the triplet and dipole as a function of the energy.

Finally, the electron charge surface density in the focal plane of the triplet and dipole associated with FIG. 10, is plotted in FIG. 11 as a function of electron energy.

As the beam size is reduced around 70 MeV, the charge surface density increases by at least a factor 3 for the energy range considered here and goes up to ≈ 0.14 pC/(MeV mm). Considering the energy at which the charge surface density is maximum and the fact that there is light dispersion in the Lanex screen, it leads to at least 2.9 pC/mm^2. This value is well below the charge saturation value ≈ 66 pC/mm^2 given by Buck et al. [51] for the Lanex screen used in this experiment. The achieved value of charge spatial and energy density can be of great interest for future applications.

4. Conclusions

In conclusion, we demonstrated that using a specifically designed magnetic line, a high charge broad band energy spectrum from 45 MeV to 150 MeV can be transported and focused about 1 m away from the source without changing the spectral properties of the electrons beam. Up to 4.7 pC can be focused to a (1.3×0.87) mm^2 spot, 1 m away from the source for electrons in energy range of 45 MeV and up to 150 MeV and a charge surface density up to 2.9 pC/mm^2 at 69$\pm$2 MeV. This magnetic line has been designed to transport and precisely diagnose electrons around 70 MeV for an electron beam without strong divergence-energy correlation, which is the case for the studied laser-plasma source. This type of magnetic ensemble offers new perspectives for applications, as it allows to work with a spatially stable electron beam (gain of a factor 3 on the position stability of the beam), and 1 m away from the source, reducing considerably the impact of the co-propagating laser pulse. This transport line and dipole is also an energy diagnostic for electrons with a very good energy resolution around the reference energy (down to less than 1% at 69.4 MeV in this case).

5. Acknowledgments

This work was supported by Triangle de la physique under contract No. 2011-086T MULTIPLACCELE, No.2012-032ELISA and DACTOMUS project was financed by the LabEX P2IO. We acknowledge the help of D. Garzella, C. Pothier and F. Réau for UHI100 laser operation. The research leading to these results has received funding from LASERLAB-EUROPE (grant agreement no. 654148, European Union's Horizon 2020 research and innovation program).

References

[1] C. G. R. Geddes, C. Toth, J. van Tilborg, E. Esarey, C. B. Schroeder, D. Bruhwiler, C. Nieter, J. Cary, W. P. Leemans, High-quality electron beams from a laser wakefield accelerator using plasma-channel guiding, Nature 431 (7008) (2004) 538–541. doi:10.1038/nature02900.
URL http://www.nature.com/nature/journal/v431/n7008/abs/nature02900.html

[2] J. Faure, Y. Glinec, A. Pukhov, S. Kiselev, S. Gordienko, E. Lefebvre, J.-P. Rousseau, F. Burgy, V. Malka, A laser–plasma accelerator producing monoenergetic electron beams, Nature 431 (7008) (2004) 541–544. doi:10.1038/nature02963.
URL http://www.nature.com/nature/journal/v431/n7008/abs/nature02963.html

[3] S. P. D. Mangles, C. D. Murphy, Z. Najmudin, A. G. R. Thomas, J. L. Collier, A. E. Dangor, E. J. Divall, P. S. Foster, J. G. Gallacher, C. J. Hooker, D. A. Jaroszynski, A. J. Langley, W. B. Mori, P. A. Norreys, F. S. Tsung, R. Viskup, B. R. Walton, K. Krushelnick, Monoenergetic beams of relativistic electrons from intense laser–plasma interactions, Nature 431 (7008) (2004) 535–538. doi:10.1038/nature02939.
URL http://www.nature.com/nature/journal/v431/n7008/abs/nature02939.html

[4] T. Tajima, J. M. Dawson, Laser Electron Accelerator, Phys Rev Lett 43 (4) (1979) 267–270. doi:10.1103/PhysRevLett.43.267.
URL http://link.aps.org/doi/10.1103/PhysRevLett.43.267

[5] C. McGuffey, A. G. R. Thomas, W. Schumaker, T. Matsuoka, V. Chvykov, F. J. Dollar, G. Kalintchenko, V. Yanovsky, A. Maksimchuk, K. Krushelnick, V. Y. Bychenkov, I. V. Glazyrin, A. V. Karpeev, Ionization Induced Trapping in a Laser Wakefield Accelerator, Phys Rev Lett 104 (2) (2010) 025004, wOS:000274002900032. doi:10.1103/PhysRevLett.104.025004.

[6] A. Pak, K. A. Marsh, S. F. Martins, W. Lu, W. B. Mori, C. Joshi, Injection and Trapping of Tunnel-Ionized Electrons into Laser-Produced Wakes, Phys Rev Lett 104 (2) (2010) 025003. doi:10.1103/PhysRevLett.104.025003.

URL http://link.aps.org/doi/10.1103/PhysRevLett.104.025003

[7] M. Chen, E. Esarey, C. B. Schroeder, C. G. R. Geddes, W. P. Leemans, Theory of ionization-induced trapping in laser-plasma accelerators, Physics of Plasmas (1994-present) 19 (3) (2012) 033101. doi:10.1063/1.3689922.

URL http://scitation.aip.org/content/aip/journal/pop/19/3/10.1063/1.3689922

[8] J. Faure, C. Rechatin, A. Norlin, A. Lifschitz, Y. Glinec, V. Malka, Controlled injection and acceleration of electrons in plasma wakefields by colliding laser pulses, Nature 444 (7120) (2006) 737–739. doi:10.1038/nature05393.

URL http://www.nature.com/nature/journal/v444/n7120/abs/nature05393.html

[9] M. Burza, A. Gonoskov, K. Svensson, F. Wojda, A. Persson, M. Hansson, G. Genoud, M. Marklund, C.-G. Wahlström, O. Lundh, Laser wakefield acceleration using wire produced double density ramps, Physical Review Special Topics - Accelerators and Beams 16 (1) (2013) 011301. doi:10.1103/PhysRevSTAB.16.011301.

URL http://link.aps.org/doi/10.1103/PhysRevSTAB.16.011301

[10] K. Schmid, A. Buck, C. M. S. Sears, J. M. Mikhailova, R. Tautz, D. Herrmann, M. Geissler, F. Krausz, L. Veisz, Density-transition based electron injector for laser driven wakefield accelerators, Physical Review Special Topics - Accelerators and Beams 13 (9) (2010) 091301. doi:10.1103/PhysRevSTAB.13.091301.

URL http://link.aps.org/doi/10.1103/PhysRevSTAB.13.091301

[11] A. J. Gonsalves, K. Nakamura, C. Lin, D. Panasenko, S. Shiraishi, T. Sokollik, C. Benedetti, C. B. Schroeder, C. G. R. Geddes, J. van Tilborg, J. Osterhoff, E. Esarey, C. Toth, W. P. Leemans, Tunable laser plasma accelerator based on longitudinal density tailoring, Nature Physics 7 (11) (2011) 862–866. doi:10.1038/nphys2071.

URL http://www.nature.com/nphys/journal/v7/n11/abs/nphys2071.html

[12] B. B. Pollock, C. E. Clayton, J. E. Ralph, F. Albert, A. Davidson, L. Divol, C. Filip, S. H. Glenzer, K. Herpoldt, W. Lu, K. A. Marsh, J. Meinecke, W. B. Mori, A. Pak, T. C. Rensink, J. S. Ross, J. Shaw, G. R. Tynan, C. Joshi, D. H. Froula, Demonstration of a Narrow Energy Spread, $\approx 0.5 GeV$ Electron Beam from a Two-Stage Laser Wakefield Accelerator, Phys Rev Lett 107 (4) (2011) 045001.

doi:10.1103/PhysRevLett.107.045001.

URL http://link.aps.org/doi/10.1103/PhysRevLett.107.045001

[13] W. Wang, W. Li, J. Liu, C. Wang, Q. Chen, Z. Zhang, R. Qi, Y. Leng, X. Liang, Y. Liu, X. Lu, C. Wang, R. Li, Z. Xu, Control of seeding phase for a cascaded laser wakefield accelerator with gradient injection, Appl Phys Lett 103 (24) (2013) 243501. doi:10.1063/1.4842236.

URL http://scitation.aip.org/content/aip/journal/apl/103/24/10.1063/1.4842236

[14] J. S. Liu, C. Q. Xia, W. T. Wang, H. Y. Lu, C. Wang, A. H. Deng, W. T. Li, H. Zhang, X. Y. Liang, Y. X. Leng, X. M. Lu, C. Wang, J. Z. Wang, K. Nakajima, R. X. Li, Z. Z. Xu, All-Optical Cascaded Laser Wakefield Accelerator Using Ionization-Induced Injection, Phys Rev Lett 107 (3) (2011) 035001. doi:10.1103/PhysRevLett.107.035001.

URL http://link.aps.org/doi/10.1103/PhysRevLett.107.035001

[15] I. Dornmair, K. Floettmann, A. Maier, Emittance conservation by tailored focusing profiles in a plasma accelerator, Physical Review Special Topics - Accelerators and Beams 18 (4) (2015) 041302. doi:10.1103/PhysRevSTAB.18.041302.

URL https://link.aps.org/doi/10.1103/PhysRevSTAB.18.041302

[16] X. Xu, J. Hua, Y. Wu, C. Zhang, F. Li, Y. Wan, C.-H. Pai, W. Lu, W. An, P. Yu, M. Hogan, C. Joshi, W. Mori, Physics of Phase Space Matching for Staging Plasma and Traditional Accelerator Components Using Longitudinally Tailored Plasma Profiles, Physical Review Letters 116 (12) (2016) 124801. doi:10.1103/PhysRevLett.116.124801.

URL https://link.aps.org/doi/10.1103/PhysRevLett.116.124801

[17] M. Fuchs, R. Weingartner, A. Popp, Z. Major, S. Becker, J. Osterhoff, I. Cortrie, B. Zeitler, R. Hörlein, G. D. Tsakiris, U. Schramm, T. P. Rowlands-Rees, S. M. Hooker, D. Habs, F. Krausz, S. Karsch, F. Grüner, Laser-driven soft-X-ray undulator source, Nature Physics 5 (11) (2009) 826–829. doi:10.1038/nphys1404.

URL http://www.nature.com/nphys/journal/v5/n11/full/nphys1404.html

[18] S. Chen, N. D. Powers, I. Ghebregziabher, C. M. Maharjan, C. Liu, G. Golovin, S. Banerjee, J. Zhang, N. Cunningham, A. Moorti, S. Clarke, S. Pozzi, D. P. Umstadter, MeV-Energy X Rays from Inverse Compton Scattering with Laser-Wakefield Accelerated Electrons, Phys Rev Lett 110 (15) (2013) 155003. doi:10.1103/PhysRevLett.110.155003.

URL http://link.aps.org/doi/10.1103/PhysRevLett.110.155003

[19] T. Fuchs, H. Szymanowski, U. Oelfke, Y. Glinec, C. Rechatin, J. Faure, V. Malka, Treatment planning

for laser-accelerated very-high energy electrons, Physics in Medicine and Biology 54 (11) (2009) 3315. doi:10.1088/0031-9155/54/11/003.

URL http://stacks.iop.org/0031-9155/54/i=11/a=003

[20] C. DesRosiers, V. Moskvin, A. F. Bielajew, L. Papiez, 150-250 meV electron beams in radiation therapy, Physics in Medicine and Biology 45 (7) (2000) 1781–1805.

[21] C. Yeboah, G. A. Sandison, V. Moskvin, Optimization of intensity-modulated very high energy (50–250 MeV) electron therapy, Physics in Medicine and Biology 47 (8) (2002) 1285. doi:10.1088/0031-9155/47/8/305.

URL http://stacks.iop.org/0031-9155/47/i=8/a=305

[22] V. Malka, A. Lifschitz, J. Faure, Y. Glinec, Staged concept of laser-plasma acceleration toward multi-GeV electron beams, Physical Review Special Topics - Accelerators and Beams 9 (9) (2006) 091301. doi:10.1103/PhysRevSTAB.9.091301.

URL http://link.aps.org/doi/10.1103/PhysRevSTAB.9.091301

[23] A. J. W. Reitsma, W. P. Leemans, E. Esarey, C. B. Schroeder, L. P. J. Kamp, T. J. Schep, Simulation of electron postacceleration in a two-stage laser wakefield accelerator, Physical Review Special Topics - Accelerators and Beams 5 (5) (2002) 051301. doi:10.1103/PhysRevSTAB.5.051301.

URL http://link.aps.org/doi/10.1103/PhysRevSTAB.5.051301

[24] B. Cros, B. S. Paradkar, X. Davoine, A. Chancé, F. G. Desforges, S. Dobosz-Dufrénoy, N. Delerue, J. Ju, T. L. Audet, G. Maynard, M. Lobet, L. Gremillet, P. Mora, J. Schwindling, O. Delferrière, C. Bruni, C. Rimbault, T. Vinatier, A. Di Piazza, M. Grech, C. Riconda, J. R. Marquès, A. Beck, A. Specka, P. Martin, P. Monot, D. Normand, F. Mathieu, P. Audebert, F. Amiranoff, Laser plasma acceleration of electrons with multi-PW laser beams in the frame of CILEX, Nuclear Instruments and Methods in Physics Research A 740 (2014) 27–33. doi:10.1016/j.nima.2013.10.090.

URL http://adsabs.harvard.edu/abs/2014NIMPA.740...27C

[25] S. Steinke, J. van Tilborg, C. Benedetti, C. G. R. Geddes, C. B. Schroeder, J. Daniels, K. K. Swanson, A. J. Gonsalves, K. Nakamura, N. H. Matlis, B. H. Shaw, E. Esarey, W. P. Leemans, Multistage coupling of independent laser-plasma accelerators, Nature 530 (7589) (2016) 190–193. doi:10.1038/nature16525.

[26] S. P. D. Mangles, A. G. R. Thomas, M. C. Kaluza, O. Lundh, F. Lindau, A. Persson, Z. Najmudin, C.-G. Wahlström, C. D. Murphy, C. Kamperidis, K. L. Lancaster, E. Divall, K. Krushelnick, Effect of laser contrast ratio on electron beam stability in laser wakefield acceleration experiments, Plasma

Physics and Controlled Fusion 48 (12B) (2006) B83. doi:10.1088/0741-3335/48/12B/S08.
URL http://stacks.iop.org/0741-3335/48/i=12B/a=S08

[27] M. Vargas, W. Schumaker, Z.-H. He, Z. Zhao, K. Behm, V. Chvykov, B. Hou, K. Krushelnick, A. Maksimchuk, V. Yanovsky, A. G. R. Thomas, Improvements to laser wakefield accelerated electron beam stability, divergence, and energy spread using three-dimensional printed two-stage gas cell targets, Applied Physics Letters 104 (17) (2014) 174103. doi:10.1063/1.4874981.
URL http://aip.scitation.org/doi/10.1063/1.4874981

[28] S. P. D. Mangles, A. G. R. Thomas, O. Lundh, F. Lindau, M. C. Kaluza, A. Persson, C.-G. Wahlström, K. Krushelnick, Z. Najmudin, On the stability of laser wakefield electron accelerators in the monoenergetic regime, Physics of Plasmas 14 (5) (2007) 056702. doi:10.1063/1.2436481.
URL http://aip.scitation.org/doi/abs/10.1063/1.2436481

[29] S. Banerjee, S. Y. Kalmykov, N. D. Powers, G. Golovin, V. Ramanathan, N. J. Cunningham, K. J. Brown, S. Chen, I. Ghebregziabher, B. A. Shadwick, others, Stable, tunable, quasimonoenergetic electron beams produced in a laser wakefield near the threshold for self-injection, Physical Review Special Topics-Accelerators and Beams 16 (3) (2013) 031302.
URL http://journals.aps.org/prstab/abstract/10.1103/PhysRevSTAB.16.031302

[30] C. Thaury, E. Guillaume, A. Döpp, R. Lehe, A. Lifschitz, K. Ta Phuoc, J. Gautier, J.-P. Goddet, A. Tafzi, A. Flacco, F. Tissandier, S. Sebban, A. Rousse, V. Malka, Demonstration of relativistic electron beam focusing by a laser-plasma lens, Nature Communications 6 (2015) 6860. doi:10.1038/ncomms7860.
URL http://www.nature.com/ncomms/2015/150416/ncomms7860/full/ncomms7860.html

[31] J. van Tilborg, S. Barber, H.-E. Tsai, K. Swanson, S. Steinke, C. Geddes, A. Gonsalves, C. Schroeder, E. Esarey, S. Bulanov, N. Bobrova, P. Sasorov, W. Leemans, Nonuniform discharge currents in active plasma lenses, Physical Review Accelerators and Beams 20 (3) (2017) 032803. doi:10.1103/PhysRevAccelBeams.20.032803.
URL https://link.aps.org/doi/10.1103/PhysRevAccelBeams.20.032803

[32] S. M. Wiggins, R. C. Issac, G. H. Welsh, E. Brunetti, R. P. Shanks, M. P. Anania, S. Cipiccia, G. G. Manahan, C Aniculaesei, B. Ersfeld, M. R. Islam, R. T. L. Burgess, G. Vieux, W. A. Gillespie, A. M. MacLeod, S. B. v. d. Geer, M. J. d. Loos, D. A. Jaroszynski, High quality electron beams from a laser wakefield accelerator, Plasma Physics and Controlled Fusion 52 (12) (2010) 124032. doi:10.1088/0741-3335/52/12/124032.

URL http://stacks.iop.org/0741-3335/52/i=12/a=124032

[33] M. P. Anania, E. Brunetti, S. M. Wiggins, D. W. Grant, G. H. Welsh, R. C. Issac, S. Cipiccia, R. P. Shanks, G. G. Manahan, C. Aniculaesei, S. B. v. d. Geer, M. J. d. Loos, M. W. Poole, B. J. A. Shepherd, J. A. Clarke, W. A. Gillespie, A. M. MacLeod, D. A. Jaroszynski, An ultrashort pulse ultra-violet radiation undulator source driven by a laser plasma wakefield accelerator, Appl Phys Lett 104 (26) (2014) 264102. doi:10.1063/1.4886997.

URL http://scitation.aip.org/content/aip/journal/apl/104/26/10.1063/1.4886997

[34] G. G. Manahan, E. Brunetti, C. Aniculaesei, M. P. Anania, S. Cipiccia, M. R. Islam, D. W. Grant, A. Subiel, R. P. Shanks, R. C. Issac, G. H. Welsh, S. M. Wiggins, D. A. Jaroszynski, Characterization of laser-driven single and double electron bunches with a permanent magnet quadrupole triplet and pepper-pot mask, New Journal of Physics 16 (2014) 103006, wOS:000344094100004. doi:10.1088/1367-2630/16/10/103006.

[35] T. Eichner, F. Grüner, S. Becker, M. Fuchs, D. Habs, R. Weingartner, U. Schramm, H. Backe, P. Kunz, W. Lauth, Miniature magnetic devices for laser-based, table-top free-electron lasers, Physical Review Special Topics - Accelerators and Beams 10 (8) (2007) 082401. doi:10.1103/PhysRevSTAB.10.082401.

URL http://link.aps.org/doi/10.1103/PhysRevSTAB.10.082401

[36] R. Weingartner, M. Fuchs, A. Popp, S. Raith, S. Becker, S. W. Chou, M. Heigoldt, K. Khrennikov, J. Wenz, T. Seggebrock, B. Zeitler, Z. Major, J. Osterhoff, F. Krausz, S. Karsch, F. Grüner, Imaging laser-wakefield-accelerated electrons using miniature magnetic quadrupole lenses, Physical Review Special Topics - Accelerators and Beams 14 (5). doi:10.1103/PhysRevSTAB.14.052801.

URL http://prst-ab.aps.org/abstract/PRSTAB/v14/i5/e052801

[37] S. Barber, J. van Tilborg, C. Schroeder, R. Lehe, H.-E. Tsai, K. Swanson, S. Steinke, K. Nakamura, C. Geddes, C. Benedetti, E. Esarey, W. Leemans, Measured Emittance Dependence on the Injection Method in Laser Plasma Accelerators, Physical Review Letters 119 (10) (2017) 104801. doi:10.1103/PhysRevLett.119.104801.

URL https://link.aps.org/doi/10.1103/PhysRevLett.119.104801

[38] T. André, I. A. Andriyash, A. Loulergue, M. Labat, E. Roussel, A. Ghaith, M. Khojoyan, C. Thaury, M. Valléau, F. Briquez, F. Marteau, K. Tavakoli, P. N'Gotta, Y. Dietrich, G. Lambert, V. Malka, C. Benabderrahmane, J. Vétéran, L. Chapuis, T. E. Ajjouri, M. Sebdaoui, N. Hubert, O. Marcouillé, P. Berteaud, N. Leclercq, M. E. Ajjouri, P. Rommeluère, F. Bouvet, J.-P. Duval, C. Kitegi, F. Blache, B. Mahieu, S. Corde, J. Gautier, K. T. Phuoc, J. P. Goddet, A. Lestrade, C. Herbeaux, C. Évain,

C. Szwaj, S. Bielawski, A. Tafzi, P. Rousseau, S. Smartsev, F. Polack, D. Dennetière, C. Bourassin-Bouchet, C. D. Oliveira, M.-E. Couprie, Control of laser plasma accelerated electrons for light sources, Nature Communications 9 (1) (2018) 1334. doi:10.1038/s41467-018-03776-x.
URL https://www.nature.com/articles/s41467-018-03776-x

[39] Z.-H. He, B. Beaurepaire, J. A. Nees, G. Gallé, S. A. Scott, J. R. S. Pérez, M. G. Lagally, K. Krushelnick, A. G. R. Thomas, J. Faure, Capturing Structural Dynamics in Crystalline Silicon Using Chirped Electrons from a Laser Wakefield Accelerator, Scientific Reports 6 (2016) 36224.
URL http://dx.doi.org/10.1038/srep36224

[40] T. L. Audet, M. Hansson, P. Lee, F. G. Desforges, G. Maynard, S. D. Dufrénoy, R. Lehe, J.-L. Vay, B. Aurand, A. Persson, I. G. González, A. Maitrallain, P. Monot, C.-G. Wahlström, O. Lundh, B. Cros, Investigation of ionization-induced electron injection in a wakefield driven by laser inside a gas cell, Physics of Plasmas 23 (2) (2016) 023110. doi:10.1063/1.4942033.
URL http://scitation.aip.org/content/aip/journal/pop/23/2/10.1063/1.4942033

[41] T. L. Audet, F. G. Desforges, A. Maitrallain, S. D. Dufrénoy, M. Bougeard, G. Maynard, P. Lee, M. Hansson, B. Aurand, A. Persson, I. G. González, P. Monot, C. G. Wahlström, O. Lundh, B. Cros, Electron injector for compact staged high energy accelerator, Nucl Instrum and Methods in Physics Research Section A 829 (2016) 304–308. doi:10.1016/j.nima.2016.01.035.
URL https://www.sciencedirect.com/science/article/pii/S0168900216000516

[42] T. L. Audet, P. Lee, G. Maynard, S. D. Dufrénoy, A. Maitrallain, M. Bougeard, P. Monot, B. Cros, Gas cell density characterization for laser wakefield acceleration, Nuclear Instruments and Methods in Physics Research Section A: Accelerators, Spectrometers, Detectors and Associated Equipmentdoi:https://doi.org/10.1016/j.nima.2018.01.053.
URL http://www.sciencedirect.com/science/article/pii/S0168900218300706

[43] D. Papadopoulos, J. Zou, C. Le Blanc, G. Chériaux, P. Georges, F. Druon, G. Mennerat, P. Ramirez, L. Martin, A. Fréneaux, et al., The apollon 10 pw laser: experimental and theoretical investigation of the temporal characteristics, High Power Laser Science and Engineering 4. doi:10.1017/hpl.2016.34.

[44] OPERA, OPERA-3D Reference Manual, Vector Fields Ltd.

[45] Tracewin documentation (2016).
URL http://irfu.cea.fr/Sacm/logiciels/index.php

[46] Y. Hayakawa, F. E. Eraso, W. C. Scarfe, A. G. Farman, K. Nishikawa, K. Kuroyanagi, M. Smith, Technical note. Modulation transfer function analysis of a newly revised rotational panoramic machine,

Dento Maxillo Facial Radiology 25 (5) (1996) 302–306. doi:10.1259/dmfr.25.5.9161187.

[47] A. K. E. Omar, G. Baldacchino, I. Monnet, P. Bouniol, Revisited water radiolysis at elevated pH by accounting $O_3^{\cdot -}$ kinetics at low and high LET, RSC Advances 5 (108) (2015) 89244–89253. doi:10.1039/C5RA16858A.

URL http://pubs.rsc.org/en/content/articlelanding/2015/ra/c5ra16858a

[48] S. P. D. Mangles, A. G. R. Thomas, M. C. Kaluza, O. Lundh, F. Lindau, A. Persson, F. S. Tsung, Z. Najmudin, W. B. Mori, C.-G. Wahlström, K. Krushelnick, Laser-Wakefield Acceleration of Monoenergetic Electron Beams in the First Plasma-Wave Period, Phys Rev Lett 96 (21) (2006) 215001. doi:10.1103/PhysRevLett.96.215001.

URL http://link.aps.org/doi/10.1103/PhysRevLett.96.215001

[49] P. Lee, G. Maynard, T. Audet, B. Cros, R. Lehe, J.-L. Vay, Dynamics of electron injection and acceleration driven by laser wakefield in tailored density profiles, Physical Review Accelerators and Beams 19 (11) (2016) 112802. doi:10.1103/PhysRevAccelBeams.19.112802.

URL https://link.aps.org/doi/10.1103/PhysRevAccelBeams.19.112802

[50] R. Weingartner, S. Raith, A. Popp, S. Chou, J. Wenz, K. Khrennikov, M. Heigoldt, A. R. Maier, N. Kajumba, M. Fuchs, B. Zeitler, F. Krausz, S. Karsch, F. Grüner, Ultralow emittance electron beams from a laser-wakefield accelerator, Physical Review Special Topics - Accelerators and Beams 15 (11) (2012) 111302. doi:10.1103/PhysRevSTAB.15.111302.

URL https://link.aps.org/doi/10.1103/PhysRevSTAB.15.111302

[51] A. Buck, K. Zeil, A. Popp, K. Schmid, A. Jochmann, S. D. Kraft, B. Hidding, T. Kudyakov, C. M. S. Sears, L. Veisz, S. Karsch, J. Pawelke, R. Sauerbrey, T. Cowan, F. Krausz, U. Schramm, Absolute charge calibration of scintillating screens for relativistic electron detection, Rev Sci Instrum 81 (3) (2010) 033301. doi:10.1063/1.3310275.